

# A versatile solution for the gravity anomaly of 3D prism-meshed bodies with depth-dependent density contrast

Li Jiang<sup>1</sup>, Jianzhong Zhang<sup>2</sup>, and Zhibing Feng<sup>1</sup>

## ABSTRACT

We have developed a generalized solution for computing the gravity anomalies of 3D irregular-mass bodies with complicated density-contrast variation. The 3D irregular-shaped bodies can be approximated flexibly by a collection of finite-juxtaposed right-rectangular prisms. The complicated density-contrast variation of each prism can be well-represented by a depth-dependent polynomial function. A novel analytic solution of gravity anomalies due to a right-rectangular prism with an arbitrary order of polynomial density-contrast function of depth is then derived. The solution is singularity free in the upper half-space over the prism, and its singularity in the lower half-space

containing the prism is resolved by assigning their limit values to the singular terms. The numerical stability of the solution is also evaluated through numerical tests. Hence, the solution can be used to compute the gravity anomalies of 3D irregular bodies with variable density contrasts without singularities when computation points are within the numerical stability range. Based on synthetic models with variable density contrast, our solution is validated by using other solutions in the literature. We also simulated the gravity anomalies of the Los Angeles basin and compared them with the observed anomalies and with those computed using the analytic solutions of other workers. These tests confirm the accuracy and efficiency of our analytic solution.

## INTRODUCTION

Computation of the gravity anomaly of an arbitrarily shaped 3D body mass is generally addressed by dividing the body into finite-juxtaposed regular-shaped bodies or building blocks with uniform density contrast. Right-rectangular prisms are often used to approximate a body with complex geometry in local gravity field modeling (Nagy, 1966; Garcia-Abdeslem, 1992). Spherical prisms or “tesseroids” were used to approximate a regional-scale body by Roussel et al. (2015). A vertical pyramid model was presented to the benefit of basin modeling by Gokula and Sastry (2015). A polyhedral body was used for computing the gravity anomalies of a 3D irregular body by Hansen (1999), Holstein (2003), and D’Urso (2014).

However, these bodies with constant density have not captured the complexities of sedimentary fill in geologic conditions. Athy (1930) points out that compaction, which was the dominant physical process during the geologic evolution of a sedimentary basin,

always led to density increasing with depth. Since then, variable-density models have been adopted in gravity computation and inversion. Some solutions were obtained for gravity anomalies due to geologic bodies with simple density-depth functions, such as linear (Prutkin and Tenzer, 2009), quadratic polynomial (Rao, 1990; Gal-lardo-Delgado et al., 2003), cubic polynomial (Garcia-Abdeslem, 2005), exponential (Chai and Hinze, 1988; Chappell and Kuszniir, 2008), hyperbolic (Litinsky, 1989; Rao et al., 1995), and parabolic (Chakravarthi et al., 2002; Gokula and Sastry, 2015). Zhou (2009) reduces the 3D integral for the gravity anomaly of a 3D prism with depth and/or horizontally dependent density-contrast function to a 1D line integral that was then solved using a numerical method.

Zhang et al. (2001) present an arbitrary-order polynomial density function of depth and horizontal distance, which is flexible to represent arbitrary variable-density distribution. The space-domain analytic solutions of gravity anomalies due to a 2D polygon body with such a polynomial density function are given by Zhang et al.

Manuscript received by the Editor 25 July 2016; revised manuscript received 6 March 2017; published online 16 May 2017.

<sup>1</sup>Ocean University of China, Key Laboratory of Submarine Geosciences and Prospecting Techniques, Ministry of Education, College of Marine Geosciences, Qingdao, China. E-mail: jianglifzb@163.com; zbfengjl@163.com.

<sup>2</sup>Ocean University of China, Key Laboratory of Submarine Geosciences and Prospecting Techniques, Ministry of Education, College of Marine Geosciences and Evaluation and Detection Technology Laboratory of Marine Mineral Resources, Qingdao National Laboratory for Marine Science and Technology, Qingdao, China. E-mail: zhangjz@ouc.edu.cn.

© 2017 Society of Exploration Geophysicists. All rights reserved.

(2001), Zhou (2010), and D'Urso (2015). Wu and Chen (2016) derive a frequency-domain solution of gravity anomalies due to a vertical rectangular prism with general polynomial density-contrast function. For the frequency-domain solution, the inverse Fourier transform has to be used to obtain the gravity anomalies, which inevitably causes truncation errors in the resulting gravity anomalies.

Consider that right-rectangular prisms are often used as building blocks for arbitrary-shaped 3D bodies and the computation of 3D gravity anomalies. It follows that polynomial density-contrast functions can reasonably approximate the arbitrary depth-dependent density contrast of geologic bodies, especially sedimentary basins. Given these features, in this paper, we focus on deriving an analytic

solution for the gravity anomalies caused by a right-rectangular prism with a depth-dependent polynomial density contrast, with which the gravity anomalies due to arbitrary-shaped 3D bodies with complicated density-contrast variation can be computed. The singularity and numerical instability problems of the analytic solution are also analyzed. The analytic solution proposed here is then validated against other numerical and analytic solutions using synthetic models and observed data in the Los Angeles Basin.

## POLYNOMIAL DENSITY-CONTRAST FUNCTION

The density contrasts of sedimentary rocks generally decrease with depth. The variations of the density contrasts with depth are often different among sedimentary basins. Different mathematical functions were used to simulate the variations of density contrast with depth in different basins. For example, Chai and Hinze (1988) and Rao et al. (1995) build the exponential and the hyperbolic density-contrast models in San Jacinto Graben, respectively. Chakravarthi et al. (2002) use the parabolic density-contrast model in Los Angeles Basin. These density-contrast functions are listed in Table 1, and their curves are shown in Figure 1.

Mathematically, any rational function can be approximated by a high-order polynomial function. Thus, we use a polynomial function to approximate the variation of density contrast with depth. Figure 1 shows that fourth-order polynomial density-contrast functions with different coefficients (listed in Table 1) fit well the exponential (solid line), the hyperbolic (dashed line), and the parabolic (dotted-dashed line) density-contrast curves.

Moreover, the polynomial functions can fit more complicated density-contrast variations. For example, the density varies with depth at well E16-03 on the offshore Cleaverbank Platform from the density-log data in Verweij et al. (2016). The density has a relatively low value at shallower depth owing to high porosities in sediments recently deposited, then increases with depth, and decreases abruptly at approximately 2–3 km depth owing to the Zechstein salt structures. The density contrasts, logged as density minus 2.67 g/cm<sup>3</sup>, are shown by the solid line in Figure 2. We used the exponential and polynomial functions with different orders to fit the density-contrast data by least squares. The exponential, third-, fifth-, and seventh-order polynomial density-contrast function curves are shown in Figure 2. The higher order polynomial density-contrast function can fit more appropriately the complex density-contrast variation. Another example is the measured density-contrast curve from Phillips Petroleum A-1, Huachuca State well in the Upper San Pedro Valley, Cochise County, southeastern Arizona from the USGS, varying abruptly at some depths (the solid line in Figure 3). The eighth-order polynomial density-contrast function (the dashed line with stars in Figure 3) can match well the complicated density-contrast variation. So general polynomial functions are appropriate and flexible to represent arbitrary density-contrast variations (Zhang et al., 2001; D'Urso, 2015; Wu and Chen, 2016). Therefore, we represent a density-contrast variation with depth using an arbitrary-order polynomial function, as follows:

**Table 1. Density-contrast functions in the basins ( $\zeta$  is the depth in km, and  $\Delta\rho$  is the density contrast in g/cm<sup>3</sup>).**

Basin	Authors and their functions	Our polynomial functions
San Jacinto Graben	Chai and Hinze (1988) $\Delta\rho(\zeta) = -0.08 - 0.42e^{-0.522\zeta}$	$\Delta\rho(\zeta) = -0.5 + 2.1867 \times 10^{-1}\zeta - 5.5662 \times 10^{-2}\zeta^2 + 8.3975 \times 10^{-3}\zeta^3 - 6.1214 \times 10^{-4}\zeta^4, 0 \leq \zeta \leq 3$
San Jacinto Graben	Rao et al. (1995) $\Delta\rho(\zeta) = -0.559 \times \frac{3.098^2}{(\zeta + 3.098)^2}$	$\Delta\rho(\zeta) = -0.5585 + 3.5026 \times 10^{-1}\zeta - 1.4158 \times 10^{-1}\zeta^2 + 3.4359 \times 10^{-2}\zeta^3 - 3.5857 \times 10^{-3}\zeta^4, 0 \leq \zeta \leq 3$
Los Angeles Basin	Chakravarthi et al. (2002) $\Delta\rho(\zeta) = \frac{-0.5206^3}{(-0.5206 - 0.0576\zeta)^2}$	$\Delta\rho(\zeta) = -0.5193 + 1.1001 \times 10^{-1}\zeta - 1.4556 \times 10^{-2}\zeta^2 + 1.1192 \times 10^{-3}\zeta^3 - 3.6263 \times 10^{-5}\zeta^4, 0 \leq \zeta \leq 10$

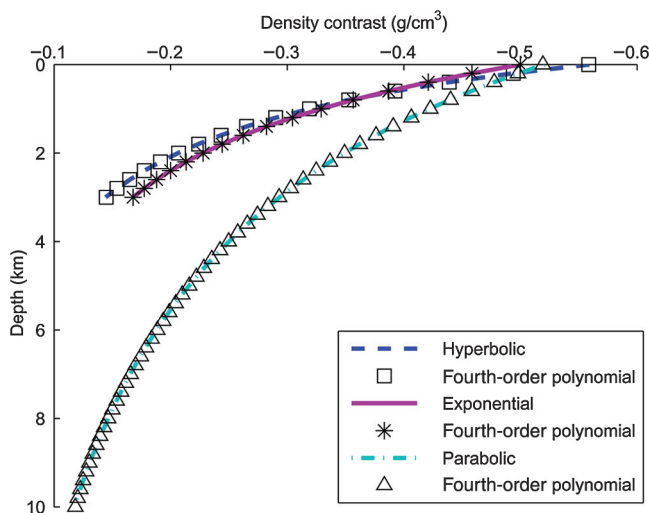


Figure 1. Variable density-contrast curves approximated using fourth-order polynomial density-contrast functions. The dashed line denotes the hyperbolic density-contrast curve in San Jacinto Graben (Rao et al., 1995), the solid line denotes the exponential density-contrast curve in San Jacinto Graben (Chai and Hinze, 1988), and the dotted-dashed line denotes the parabolic density-contrast curve in the Los Angeles Basin (Chakravarthi et al., 2002). The rectangles, stars, and triangles denote the curves of fourth-order polynomial functions with different coefficients, respectively (listed in Table 1).

$$\Delta\rho(\zeta) = \sum_{j=0}^N A_j \zeta^j, \quad (1)$$

where  $\zeta$  is the depth,  $N$  is the maximum order of  $\zeta$ , and  $A_j$  is the coefficients of the polynomial and can be estimated by a least-squares approach from the known density-depth data.

## ANALYTIC SOLUTION OF GRAVITY ANOMALY OF A RIGHT-RECTANGULAR PRISM WITH DEPTH-DEPENDENT DENSITY CONTRAST

### Expression

In a Cartesian coordinate system, by Newton's law of gravity, the gravitational anomaly at a computation point  $P(x_0, y_0, z_0)$  due to a right-rectangular prism with depth-dependent density contrast  $\Delta\rho(\zeta)$  is

$$\Delta g_z(x_0, y_0, z_0) = G \int_{\xi_1}^{\xi_2} d\xi \int_{\eta_1}^{\eta_2} d\eta \int_{\zeta_1}^{\zeta_2} \frac{\Delta\rho(\zeta)(\zeta - z_0)}{r^3} d\zeta, \quad (2)$$

where  $G$  is the gravitational constant,  $(\xi, \eta, \zeta)$  denote the coordinates of a point within the prism,  $\xi_1 \leq \xi \leq \xi_2$ ,  $\eta_1 \leq \eta \leq \eta_2$ ,  $\zeta_1 \leq \zeta \leq \zeta_2$ ,  $r = \sqrt{(\xi - x_0)^2 + (\eta - y_0)^2 + (\zeta - z_0)^2}$ , and  $\Delta\rho(\zeta)$  is given in equation 1.

Let  $x = \xi - x_0$ ,  $y = \eta - y_0$ , and  $z = \zeta - z_0$ . With binomial expansion, equation 1 can be written as

$$\Delta\rho(z) = \sum_{j=0}^N a_j z^j, \quad (3)$$

where  $a_j$  is defined as

$$a_j = \sum_{k=j}^N C_k^j A_k z_0^{k-j}, \quad j = 0, 1, \dots, N, \quad (4)$$

where  $C_k^j$  is the binomial expansion coefficients. Equation 2 can be written as

$$\Delta g_z(x_0, y_0, z_0) = G \int_{x_1}^{x_2} dx \int_{y_1}^{y_2} dy \int_{z_1}^{z_2} \frac{\Delta\rho(z)z}{r^3} dz, \quad (5)$$

where  $r = \sqrt{x^2 + y^2 + z^2}$ ,  $x_1 = \xi_1 - x_0$ ,  $x_2 = \xi_2 - x_0$ ,  $y_1 = \eta_1 - y_0$ ,  $y_2 = \eta_2 - y_0$ ,  $z_1 = \zeta_1 - z_0$ , and  $z_2 = \zeta_2 - z_0$ .

Integrating equation 5 with respect to  $x$ , we have

$$\Delta g_z(x_0, y_0, z_0) = \left[ xG \int_{y_1}^{y_2} \frac{1}{(y^2 + z^2)r} dy \int_{z_1}^{z_2} \Delta\rho(z)z dz \right]_{x_1}^{x_2}. \quad (6)$$

Applying the following equation (Guo et al., 2004):

$$\int_{y_1}^{y_2} \frac{1}{(y^2 + z^2)r} dy = \left[ -\frac{1}{xz} \arctan \frac{xz}{y^2 + z^2 + ry} \right]_{y_1}^{y_2} \quad (7)$$

to integrate equation 6 with respect to  $y$  and substituting the density-contrast function with that in equation 3, we obtain

$$\Delta g_z(x_0, y_0, z_0) = \left[ -G \sum_{j=0}^N a_j \int_{z_1}^{z_2} z^j \arctan \frac{xz}{y^2 + z^2 + ry} dz \right]_{x_1}^{x_2} \Big|_{y_1}^{y_2}. \quad (8)$$

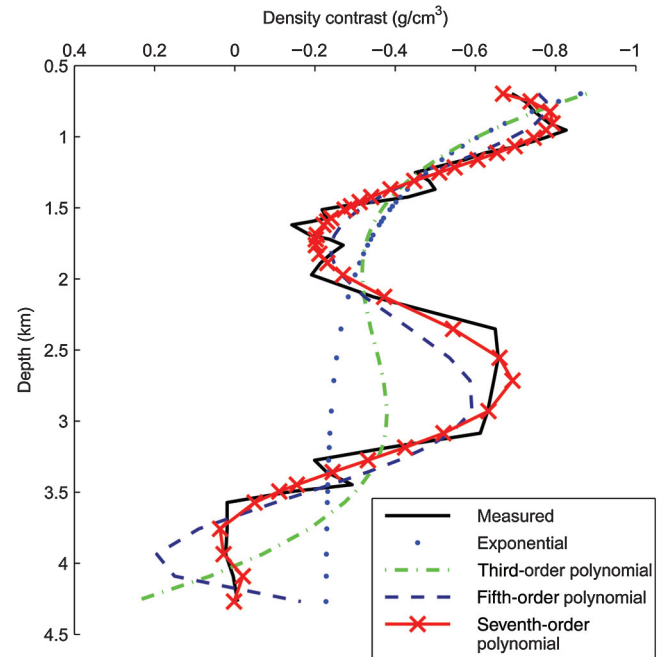


Figure 2. The fitting curves of a measured density-contrast curve using, respectively, exponential, third-, fifth-, and seventh-order polynomial functions of depth by least squares. The solid line is the measured density-contrast curve at well E16-03 on the offshore Cleaverbank Platform from the density-log data in Verweij et al. (2016). The dotted, dotted-dashed, dashed, and solid lines with crosses are the exponential, third-, fifth-, and seventh-order polynomial density-contrast function curves, respectively.

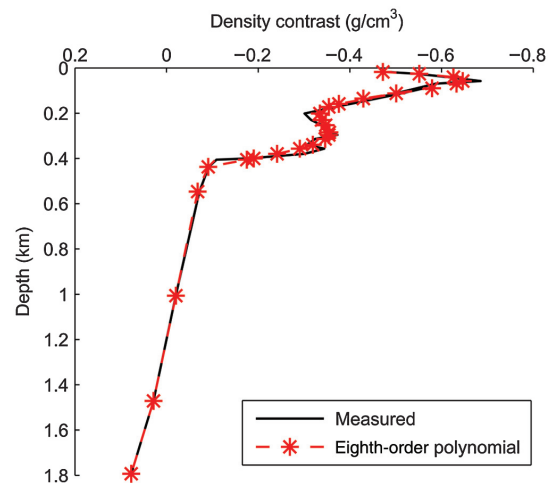


Figure 3. The approximation of a measured density-contrast curve with an eighth-order polynomial function of depth. The solid line is the measured density-contrast curve with an abrupt variation from Phillips Petroleum A-1, Huachuca State well in the Upper San Pedro Valley, Cochise County, southeastern Arizona from USGS, and the dashed line with stars denotes the eighth-order polynomial density-contrast curve.

Applying the partial integration technique, the integral in equation 8 becomes

$$\begin{aligned} & - \int_{z_1}^{z_2} z^j \arctan \frac{xz}{y^2 + z^2 + ry} dz \\ &= \left[ -\frac{z^{j+1}}{j+1} \arctan \frac{xz}{y^2 + z^2 + ry} \right] \Big|_{z_1}^{z_2} \\ &+ \frac{x}{j+1} \int_{z_1}^{z_2} \left[ \frac{y}{r(y^2 + z^2)} - \frac{1}{r(r+y)} \right] z^{j+1} dz, \\ &= \left[ -\frac{z^{j+1}}{j+1} \arctan \frac{xz}{y^2 + z^2 + ry} \right] \Big|_{z_1}^{z_2} \\ &+ \frac{xy}{j+1} \left[ \int_{z_1}^{z_2} \frac{z^{j+1}}{r(y^2 + z^2)} dz + \int_{z_1}^{z_2} \frac{z^{j+1}}{r(x^2 + z^2)} dz \right] + D, \quad (9) \end{aligned}$$

where  $D = -[x/(j+1)] \int_{z_1}^{z_2} [z^{j+1}/(x^2 + z^2)] dz$ . Because  $D$  is independent of  $y$ , definite integral  $D|_{x_1}^{x_2}|_{y_1}^{y_2}|_{z_1}^{z_2} = 0$ . When substituting equation 9 into 8,  $D$  in equation 9 can be omitted.

We solve the integrals in equation 9 in two cases:  $j$  is even and odd, respectively. If  $j$  is even, let  $j = 2m$ , for an integer  $m \geq 0$ , so

$$\begin{aligned} & \int_{z_1}^{z_2} \frac{z^{j+1}}{r(y^2 + z^2)} dz = \int_{z_1}^{z_2} \frac{(r^2 - x^2 - y^2)^m z dz}{r^2 - x^2} \frac{1}{r}, \\ &= \left| \frac{(-1)^m y^{2m}}{x} \left[ \ln(r-x) - \ln \sqrt{y^2 + z^2} \right] \right. \\ &+ \left. \sum_{l=1}^m \left[ C_m^l (-1)^{m-1} y^{2m-2l} r \sum_{w=0}^{l-1} \frac{C_{l-1}^w (-1)^w x^{2l-2w-2} r^{2w}}{2w+1} \right] \right|_{z_1}^{z_2}, \quad (10) \end{aligned}$$

and

$$\begin{aligned} & \int_{z_1}^{z_2} \frac{z^{j+1}}{r(x^2 + z^2)} dz \\ &= \left| \frac{(-1)^m x^{2m}}{y} \left[ \ln(r-y) - \ln \sqrt{x^2 + z^2} \right] \right. \\ &+ \left. \sum_{l=1}^m \left[ C_m^l (-1)^{m-1} x^{2m-2l} r \sum_{w=0}^{l-1} \frac{C_{l-1}^w (-1)^w y^{2l-2w-2} r^{2w}}{2w+1} \right] \right|_{z_1}^{z_2}. \quad (11) \end{aligned}$$

When substituting equations 10 and 11 into equation 9, the terms  $[(-1)^{m+1} y^{2m+1}/(j+1)] \ln \sqrt{y^2 + z^2}|_{z_1}^{z_2}$  and  $[(-1)^{m+1} x^{2m+1}/(j+1)] \ln \sqrt{x^2 + z^2}|_{z_1}^{z_2}$  exist with the respective lack of  $x$  and  $y$ . When substituted into equation 8, similarly to  $D$  in equation 9, they can be omitted.

If  $j$  is odd, let  $j = 2m' + 1$ , for an integer  $m' \geq 0$ , so

$$\begin{aligned} & \int_{z_1}^{z_2} \frac{z^{j+1}}{r(y^2 + z^2)} dz = \int_{z_1}^{z_2} \frac{(y^2 + z^2 - y^2)^{m'+1}}{(y^2 + z^2)r} dz, \\ &= \left[ \frac{(-1)^{m'} y^{2m'+1}}{x} \arctan \frac{xy}{y^2 + z^2 + rz} \right. \\ &+ \left. (-1)^{m'+1} (m' + 1) y^{2m'} \ln(r-z) \right] \Big|_{z_1}^{z_2} \\ &+ \sum_{u=2}^{m'+1} \left[ C_{m'+1}^u (-1)^{m'-u+1} y^{2m'-2u+2} \int_{z_1}^{z_2} \frac{(y^2 + z^2)^{u-1}}{r} dz \right], \quad (12) \end{aligned}$$

where

$$\begin{aligned} & \int_{z_1}^{z_2} \frac{(y^2 + z^2)^{u-1}}{r} dz = \int_{z_1}^{z_2} \frac{(r^2 - x^2)^{u-1}}{r} dz, \\ &= (-1)^u x^{2u-2} \ln(r-z) \Big|_{z_1}^{z_2} \\ &+ \sum_{t=1}^{u-1} \left[ C_{u-1}^t (-1)^{u-t-1} x^{2u-2t-2} \int_{z_1}^{z_2} r^{2t-1} dz \right]. \quad (13) \end{aligned}$$

Applying right-triangle equation  $r = \sqrt{x^2 + y^2} \sec \theta$ , the integral of equation 13 can be converted into

$$\int_{z_1}^{z_2} r^{2t-1} dz = (x^2 + y^2)^t \int_0^{\pi/2} (\sec \theta)^{2t+1} d\theta. \quad (14)$$

Using the indefinite integral formula (Zwillinger, 2011)

$$\begin{aligned} & \int (\sec \theta)^{2t+1} d\theta = \frac{(2t)!}{4^t (t!)^2} \\ & \times \left[ \sin \theta \sum_{v=0}^{t-1} \frac{4^v (v!)^2}{(2v+1)! \cos^{2v+2} \theta} + \ln(\sec \theta + \tan \theta) \right], \quad (15) \end{aligned}$$

and substituting equations 13 and 14 into equation 12, we have

$$\begin{aligned} & \int_{z_1}^{z_2} \frac{z^{j+1}}{r(y^2 + z^2)} dz = \left[ \frac{(-1)^{m'} y^{2m'+1}}{x} \arctan \frac{xy}{y^2 + z^2 + rz} \right. \\ &+ \left. (-1)^{m'+1} (m' + 1) y^{2m'} \ln(r-z) + \sum_{u=2}^{m'+1} I_1 \right] \Big|_{z_1}^{z_2}, \quad (16) \end{aligned}$$

where

$$\begin{aligned} & I_1 = C_{m'+1}^u (-1)^{m'} y^{2m'-2u+2} \\ & \times \left[ -x^{2u-2} \ln(r-z) + \sum_{t=1}^{u-1} C_{u-1}^t (-1)^t x^{2u-2t-2} S \right], \quad (17) \end{aligned}$$

and

$$S = \frac{(x^2 + y^2)^t (2t)!}{4^t (t!)^2} \left[ r \sum_{v=0}^{t-1} \frac{4^v (v!)^2}{(2v+1)!} \left( \frac{r^2}{x^2 + y^2} \right)^{v+1} - \ln(r-z) \right]. \quad (18)$$

In the same way, we have

$$\int_{z_1}^{z_2} \frac{z^{j+1}}{r(x^2 + z^2)} dz = \left[ \frac{(-1)^{m'} x^{2m'+1}}{y} \arctan \frac{xy}{x^2 + z^2 + rz} + (-1)^{m'+1} (m' + 1) x^{2m'} \ln(r-z) + \sum_{u=2}^{m'+1} I_2 \right] \Big|_{z_1}^{z_2}, \quad (19)$$

where

$$I_2 = C_{m'+1}^u (-1)^{m'} x^{2m'-2u+2} \times \left[ -y^{2u-2} \ln(r-z) + \sum_{t=1}^{u-1} C_{u-1}^t (-1)^t y^{2u-2t-2} S \right]. \quad (20)$$

From equations 8–11, 16, and 19, the analytic solution for gravity anomaly of a right-rectangular prism with density-contrast variation following a depth-dependent polynomial function can therefore be expressed as

$$\Delta g_z(x_0, y_0, z_0) = G \sum_{j=0}^N \frac{a_j}{j+1} \left\{ b_1 \left[ xy \sum_{l=1}^m (P_1 + P_2) + P_3 \right] + b_2 \times \left[ xy \sum_{u=2}^{m'+1} (I_1 + I_2) + I_3 \right] \right\} \Big|_{x_1}^{x_2} \Big|_{y_1}^{y_2} \Big|_{z_1}^{z_2}, \quad (21)$$

where

$$P_1 = C_m^l (-1)^{m-1} y^{2m-2l} r \sum_{w=0}^{l-1} \frac{C_{l-1}^w (-1)^w x^{2l-2w-2} r^{2w}}{2w+1}, \quad (22)$$

$$P_2 = C_m^l (-1)^{m-1} x^{2m-2l} r \sum_{w=0}^{l-1} \frac{C_{l-1}^w (-1)^w y^{2l-2w-2} r^{2w}}{2w+1}, \quad (23)$$

$$P_3 = -z^{j+1} \arctan \frac{xz}{y^2 + z^2 + ry} + (-1)^m y^{j+1} \ln(r-x) + (-1)^m x^{j+1} \ln(r-y), \quad (24)$$

$$I_1 = C_{m'+1}^u (-1)^{m'} y^{2m'-2u+2} \times \left[ -x^{2u-2} \ln(r-z) + \sum_{t=1}^{u-1} C_{u-1}^t (-1)^t x^{2u-2t-2} S \right], \quad (25)$$

$$I_2 = C_{m'+1}^u (-1)^{m'} x^{2m'-2u+2} \times \left[ -y^{2u-2} \ln(r-z) + \sum_{t=1}^{u-1} C_{u-1}^t (-1)^t y^{2u-2t-2} S \right], \quad (26)$$

$$I_3 = (-1)^{m'} x^{j+1} \arctan \frac{xy}{x^2 + z^2 + rz} + (-1)^{m'} y^{j+1} \arctan \frac{xy}{y^2 + z^2 + rz} - z^{j+1} \arctan \frac{xz}{y^2 + z^2 + ry} + (-1)^{m'+1} (m' + 1) xy (x^{j-1} + y^{j-1}) \ln(r-z), \quad (27)$$

$$S = \frac{(x^2 + y^2)^t (2t)!}{4^t (t!)^2} \left[ r \sum_{v=0}^{t-1} \frac{4^v (v!)^2}{(2v+1)!} \left( \frac{r^2}{x^2 + y^2} \right)^{v+1} - \ln(r-z) \right], \quad (28)$$

where  $m = j/2$ ,  $b_1 = 1$ , and  $b_2 = 0$ , if  $j$  is even, and  $m' = (j-1)/2$ ,  $b_1 = 0$ , and  $b_2 = 1$  if  $j$  is odd. Namely, the first term in the curly brackets on the right side of equation 22 vanishes if  $j$  is odd, and the second term vanishes if  $j$  is even. Note that the first term in the first square brackets on the right side of equation 22 is to be omitted for  $m = 0$ , and the first term in the second square brackets omitted for  $m' = 0$ .

### Singularity

Singularities generally result from the arctangent and logarithm functions in the analytic gravity expressions at some specific computation points in space (Nagy et al., 2000; Zhou, 2009). Several authors solve the singularity problem in similar gravity computations. Some avoid the singularity by excluding a small sphere around the singular points (Tsoulis and Petrovic, 2001; Zhou, 2010). Some set their limits to the terms containing indeterminate forms using L'Hospital's rules for the analytic solution at singular points (Gokula and Sastry, 2015). Holstein and Ketteridge (1996) show that in the constant density polyhedral case, all indeterminate forms have finite limiting values, so that no exclusion zones are necessary. In the linear-density case, Holstein (2003) shows that no new indeterminate cases are introduced over those already encountered in the constant-density case. Others remove the singularities of the gravity computations by using distribution theory, differential calculus, or residue theory (Kwok, 1991; D'Urso, 2013).

The arctangent functions, such as  $\arctan(xy/zr)$ ,  $\arctan(yz/xr)$ , and  $\arctan(xz/yr)$ , and the logarithm functions, such as  $\ln(r+x)$ ,  $\ln(r+y)$ , and  $\ln(r+z)$ , often appear in analytic solutions of gravity anomalies (Nagy, 1966; Rao et al., 1990; Nagy et al., 2000; Chakravarthi et al., 2002; Garcia-Abdeslem, 2005; Zhou, 2009; Commer, 2011; Chakravarthi et al., 2013). The arctangent functions are singular not only at the vertices of a prism but also on the straight lines passing through the edges of the prism in all space. According to

$$\arctan \frac{xy}{zr} \Big|_{y_1}^{y_2} = -\arctan \frac{xz}{y^2 + z^2 + ry} \Big|_{y_1}^{y_2}, \quad (29)$$

$$\arctan \frac{xz}{yr} \Big|_{z_1}^{z_2} = -\arctan \frac{xy}{y^2 + z^2 + rz} \Big|_{z_1}^{z_2}, \quad (30)$$

and



$$\arctan \frac{yz}{xr} \Big|_{z_1}^{z_2} = -\arctan \frac{xy}{x^2 + z^2 + rz} \Big|_{z_1}^{z_2}, \quad (31)$$

we adopt the arctangent functions in the right sides of the above equations in our analytic solution, which are singular only at the eight vertices of the prism. The logarithm functions  $\ln(r+x)$  and  $\ln(r+y)$  are singular on the half-lines passing through the edges of the prism in the lower source half-space, whereas  $\ln(r+z)$  is singular on the half-lines, including those in the upper nonsource half space. Owing to

$$\ln(r+z) \Big|_{z_1}^{z_2} = -\ln(r-z) \Big|_{z_1}^{z_2}, \quad (32)$$

and the logarithm function in the right side of the above equation being not singular in the upper nonsource half-space, we replace  $\ln(r+z)$  with  $-\ln(r-z)$  in our analytic solution. For the uniformity of the expressions of our analytic solution, we also replace  $\ln(r+x)$  and  $\ln(r+y)$  with  $-\ln(r-x)$  and  $-\ln(r-y)$ , respectively. In this way, our analytic solution is singularity free in the upper nonsource half-space.

Our analytic solution still has indeterminate forms at some specific points, such as eight vertices of the prism, and those on the half-lines passing through the edges of the prism in the lower source half-space. Here, we resolve the singularity of our solution by assigning their limits to the terms containing indeterminate characteristics at the singular computation points. Specifically, in the lower source half-space,

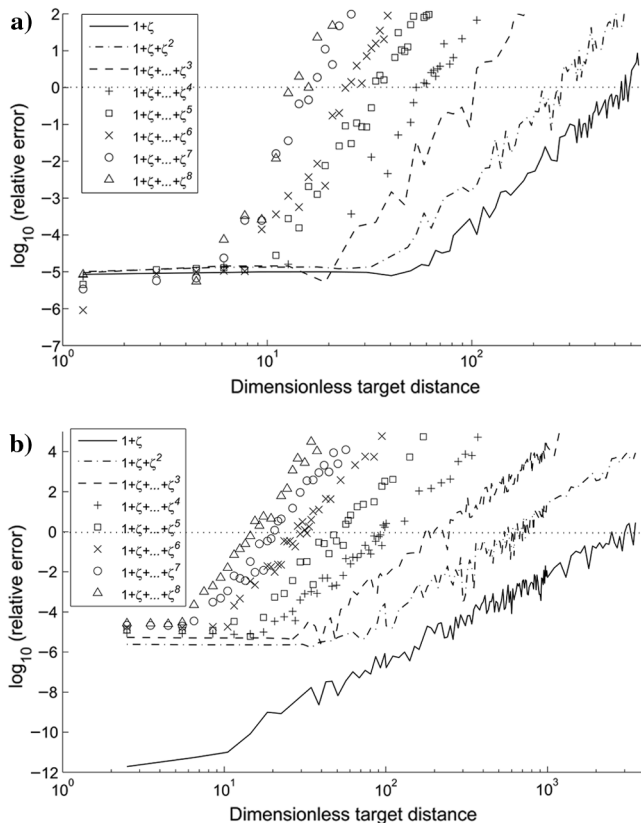


Figure 4. Numerical stability test. Logarithm of the relative errors of our solution for polynomial density-contrast functions of first to eighth orders in (a) line 2 and (b) line 3 against dimensionless target distance. The horizontal dashed line indicates the 100% relative error of our solution.

when the computation points are located at the vertices of a right-rectangular prism, their relative coordinates  $x$ ,  $y$ , and  $z$  of the each point will be zero, and thereby lead to the existence of indeterminate forms, such as  $0/0$  in the arctangent functions and  $\ln 0$  in equations 25–28. When the computation points are located on the half-lines passing through the edges of a right-rectangular prism, i.e.,  $y = z = 0$  and  $x > 0$ ,  $x = z = 0$  and  $y > 0$ , or  $x = y = 0$  and  $z > 0$ , there are indeterminate forms  $\ln 0$  in equations 25–28. Because the arctangent and logarithm functions in equations 25–28 are multiplied by the power function of  $x$ ,  $y$ , or  $z$ , the limits of the corresponding terms in equations 25–28 will be zero if the multiplier  $x$ ,  $y$ , or  $z$  equals to zero. So we can immediately assign zero to the terms containing indeterminate characteristics in equations 25–28 at the singular points, and consequently resolve the singularity problem of our analytic solution in the lower source half-space. As a result, our solution has no numerical singularities for any computation point outside, inside, and on the boundary of a right-rectangular prism.

### Numerical instability

Analytical solutions of gravity anomaly suffer from a numerical instability caused by round-off errors in computation with finite floating-point precision when the computation points are located outside a critical exploration horizon (Holstein and Ketteridge, 1996). The numerical instability was reported by Holstein and Ketteridge (1996), Holstein (2003), Zhou (2010), Holstein et al. (2014), and Wu and Chen (2016). Here, we evaluate the numerical stability of our analytic solution for 3D prisms with general polynomial density contrasts of different orders in double precision.

Our test model is the right-rectangular prism with the dimension satisfying  $0 \leq \xi \leq 1$ ,  $0 \leq \eta \leq 1$ ,  $0 \leq \zeta \leq 1$ , and with density-contrast function  $\sum_{j=0}^N \zeta^j$ . The computation points are set to be distributed in four lines. Line 1 is defined with  $x_0 \in [2, 1500]$ ,  $y_0 = 0.5$ , and  $z_0 = 0$ ; line 2 with  $x_0 = y_0$ ,  $x_0 \in [2, 800]$ , and  $z_0 = 0$ ; line 3 with  $x_0 = y_0 = z_0$  and  $z_0 \in [-3500, -2]$ ; and line 4 with  $x_0 = y_0 = 0.5$  and  $z_0 \in [-2 \times 10^5, -2]$ . The lines 1 and 2 are horizontal, and lines 3 and 4 are inclined. We calculated gravity anomalies of the test model, respectively, with first- to eighth-order polynomial density-contrast functions at the computation points using our solution and the method of approximating the prism with 100 uniform subprisms described in detail in the next section. The latter method is stable within the above computation-point range, and thus it is used as an accurate reference method.

Following Holstein and Ketteridge (1996), let  $\alpha$  be the typical linear dimension of the target body, and  $\delta$  its typical distance from a computation point. The dimensionless target distance is defined as  $\delta/\alpha$ . The critical target distance is defined as the dimensionless target distance at which the computational floating point error is of the same order as the solution; i.e., the relative error is of order unity, representing 100% actual error. Figure 4 shows the logarithm plot of the relative errors of our solution in lines 2 and 3 against increasing dimensionless target distance. The critical target distance, shown by the horizontal dashed line in Figure 4, is regarded as the operational limit of our solution. When the target distance is larger than the critical target distance, the solution will have lost all significant figures — it is totally corrupted by the effects of rounding error. Table 2 summarizes the ranges of numerical stability of our solution for various-order polynomial density-contrast functions in the four lines. The results in lines 1 and 4 suggest that the range of the numerical stability in the vertical line is much larger than that in the horizontal line for

the same order. The results in lines 2 and 3 show that the range of the numerical stability in the inclined line is larger than that in the horizontal line for the same order because some terms containing high-order power function of variables  $x$  or  $y$  and the terms containing high-order power function of  $z$  in equations 25 and 28 have the opposite positive and negative signs, adding them together leads to error cancellation. The numerical instability derives from the terms containing high-order power function of variables  $x$ ,  $y$ , or  $z$  in our solution, which magnify round-off errors in computation. The ranges of numerical stability decrease with increase of the order of polynomial density-contrast functions. For eighth-order polynomial density-contrast function, the range of numerical stability reaches a 15 target distance.

We also tested the range of numerical stability of our solution with a prism model the same as in Figure 5. The fourth-order polynomial density-contrast function in Table 1 is used, which came from the real data in the Los Angeles Basin. The stability ranges reach, respectively, a 108 target distance in line 1, defined with  $x_0 \in [400, 4 \times 10^5]$  m,  $y_0 = 200$  m, and  $z_0 = 0$ ; a 75 target distance in line 2 with  $x_0 = y_0$ ,  $x_0 \in [400, 4 \times 10^5]$  m, and  $z_0 = 0$ ; a 112 target distance in line 3 with  $x_0 = y_0 = z_0$  and  $z_0 \in [-4 \times 10^5, -400]$  m; and a 593 target distance in line 4 with  $x_0 = y_0 = 200$  m and  $z_0 \in [-2 \times 10^6, -400]$  m. The stability ranges exceed the critical target distances in the above test example for a fourth-order polynomial function in Table 2. Similarly, in practical situations, the stability range of our solution should be larger than that in Table 2 for the same order because the polynomial coefficients of the high-order terms of practical density contrast functions are very small, suppressing the magnified round-off errors. The stability range of our solution is dependent on the specific practical situation, and the results in Table 2 are only the reference values. In conclusion, for practical applications, the lowest order polynomial giving an adequate density contrast representation should be used, to keep the critical target distance as large as possible.

## TEST EXAMPLES

In this section, we implement all calculations of gravitational anomalies at points within the range of numerical stability of our solution.

### A right-rectangular prism model

For validating our analytic solution proposed in this paper, we design a right-rectangular prism model with a depth-dependent density-contrast variation, shown in Figure 5. The spatial dimension of the prism is defined by  $\xi_1 = 100$  m,  $\xi_2 = 300$  m,  $\eta_1 = 100$  m,  $\eta_2 = 300$  m,  $\zeta_1 = 0$  m, and  $\zeta_2 = 3000$  m. The computation points are placed along a measuring line, shown as the dotted-dashed line in Figure 5, which parallels  $x$ -coordinate axis and passes through the center of the top surface of the prism. The first and last points, respectively, locate at (100 m, 200 m) and (300 m, 200 m), and the interval of the points is 10 m. The parabolic density-contrast function in Table 1, defined by Chakravarthi et al. (2002) for the Los Angeles Basin modeling, is used. By fitting the parabolic density-contrast function with the least-squares fitting approach, we have the fourth-order polynomial density-contrast function in Table 1. The two density-contrast curves match well, as shown in Figure 1.

Then, we computed the gravity anomalies of the prism at the computation points by respectively using our analytic solution

with the fourth-order polynomial density-contrast function (hereafter referred to as our solution), analytic solution presented by Chakravarthi et al. (2002) with the parabolic density-contrast function (referred to as solution 1), and the method of approximating the prism with a collection of small uniform subprisms (referred to as solution 2). For solution 2, the prism with the fourth-order polynomial density-contrast function was divided into different numbers of small subprisms with different constant density contrasts, shown in Figure 5. The density contrast of each subprism was assigned the average of the density-contrast distributions in the range of depth, in which the subprism occupied. The gravity anomalies of the prism were then computed by summing the effects of all uniform subprisms.

Figure 6 shows the gravity-anomaly curves along the measuring line computed using the three solutions. The anomaly curve using our

**Table 2. Critical target distances of our solution due to a prism  $\{[\xi, \eta, \zeta]: 0 \leq \xi, \eta, \zeta \leq 1\}$  for different-order polynomial density-contrast functions in the four lines.**

$\Delta\rho(\zeta) = \sum_{j=0}^N \zeta^j$	Critical target distances			
	Line 1	Line 2	Line 3	Line 4
$N = 1$	820	540	3100	$1.1 \times 10^5$
$N = 2$	350	280	540	7500
$N = 3$	208	100	180	1400
$N = 4$	80	54	97	325
$N = 5$	54	34	57	140
$N = 6$	34	26	29	70
$N = 7$	24	18	21	39
$N = 8$	18	15	16	25

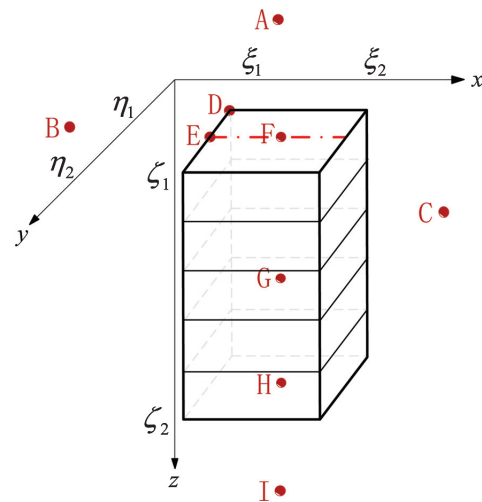


**Figure 5. A 3D rectangular prism model with depth-dependent density-contrast variation and computation points.** The prism is limited by planes  $\xi_1 = 100$  m,  $\xi_2 = 300$  m,  $\eta_1 = 100$  m,  $\eta_2 = 300$  m,  $\zeta_1 = 0$  m, and  $\zeta_2 = 3000$  m. The prism was divided into finite small uniform subprisms with different constant density contrasts for solution 2. The dotted-dashed line represents a measuring line, on which a set of computation points are placed. A, B, C, D, E, F, G, H, and I denote some special computation points.

solution (solid line) is essentially coincident with that using solution 1 (star symbols). The root-mean-square (rms) error between the two gravity anomalies is  $2.9 \times 10^{-3}$  mGal, which is caused mostly by the difference of the density-contrast functions used in the two analytic solutions. The gravity-anomaly curves computed using solution 2 with a small number of subprisms, such as 3, 5, and 20, have obvious differences with that using our solution. As the number of the subprisms increases, the gravity anomaly differences decrease. The solid line in Figure 7 shows the differences of the gravity anomalies at the computation point (200 m, 200 m, and 0 m) versus the number of the subprisms. The differences decrease rapidly from  $1.57 \times 10^{-1}$  mGal at the number of 3 to  $1.33 \times 10^{-3}$  mGal at the number of 50. When the number is greater than 50, the difference approaches zero.

The computations of the gravity anomalies were implemented using MATLAB programs on an HP Compaq Presario CQ40-609TX T4300/2.10 GHz/2 GB. For one computation point, the computation

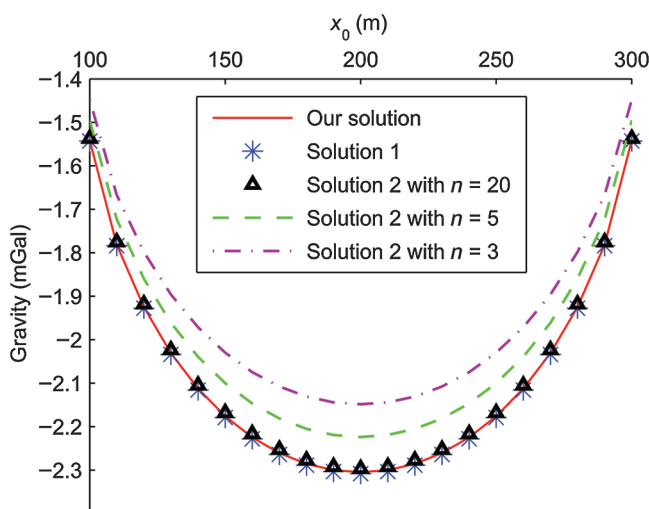


Figure 6. Gravity anomalies computed using different solutions. The solid line denotes our solution, stars denote solution 1, and dotted-dashed line, dashed line, and triangles denote solution 2 with 3, 5, and 20 subprisms, respectively.

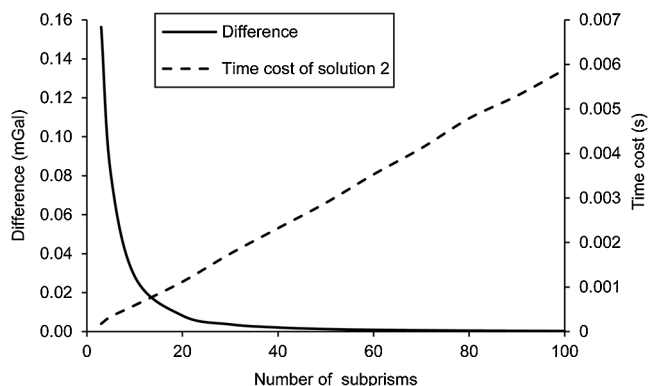


Figure 7. The differences (solid line) between the gravity anomalies computed using our solution and solution 2 at the computation point (200 m, 200 m, and 0 m) due to the prism in Figure 5, and the computation time span (dashed line) of solution 2 versus the number of the subprisms divided from the prism.

time costs using, respectively, our solution and solution 1 are almost the same, and that using solution 2 increases almost linearly with the increase of the number of the subprisms, as shown by the dashed line in Figure 7. As the number of subprisms reaches approximately 50, the computation accuracy of solution 2 is equivalent to that of our solution, but its computation time span reaches  $2.9 \times 10^{-3}$  s, or approximately 27 times of that of our solution. Consequently, our analytic solution for gravity anomalies of a prism with the general polynomial density-contrast function of depth is valid within the numerical stability range and is superior to solution 2, a common method of summing the effects of a collection of subprisms, in both computation time cost and accuracy.

To validate the singularity-free solution presented here, we then made a comparative test using our solution and solution 2 at nine computation points labeled A, B, C, D, E, F, G, H, and I, respectively, shown in Figure 5. Point A is in the air above the prism, imitating an airborne observation. Points B, C, D, E, and F are around or on the top facet of the prism, imitating the observation on undulating topography. Point D is at a vertex of the top facet of

**Table 3. The comparison of gravity anomalies computed using our solution ( $\Delta g_1$ ) and solution 2 with 50 subprisms ( $\Delta g_2$ ) at points A, B, C, D, E, F, G, H, and I in Figure 5.  $\Delta g_1 - \Delta g_2$  denotes the difference between them. The gravity anomaly and the difference are in milligals, and  $x_0$ ,  $y_0$ , and  $z_0$  are in meters.**

Point and its position ( $x_0, y_0, z_0$ )	$\Delta g_1$	$\Delta g_2$	$\Delta g_1 - \Delta g_2$
A (200, 200, -2000)	-0.034	-0.034	$-1.36 \times 10^{-6}$
B (-200, 200, 300)	-0.1721	-0.1721	$2.56 \times 10^{-5}$
C (600, 200, 1400)	0.0345	0.0345	$4.37 \times 10^{-6}$
D (100, 100, 0)	-1.1033	-1.103	$-3.22 \times 10^{-4}$
E (100, 200, 0)	-1.5411	-1.5404	$-6.59 \times 10^{-4}$
F (200, 200, 0)	-2.305	-2.3037	$-1.3 \times 10^{-3}$
G (200, 200, 1500)	0.1091	0.1109	$-1.8 \times 10^{-3}$
H (200, 200, 3000)	1.4035	1.4041	$-6.39 \times 10^{-4}$
I (200, 200, 5000)	0.0287	0.0287	$-1.16 \times 10^{-6}$

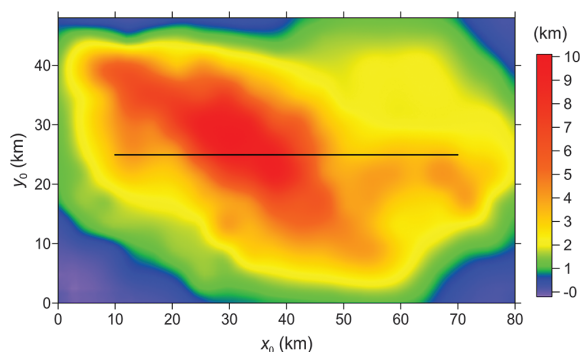


Figure 8. Depth contour of the basement interface of the Los Angeles Basin (from Chakravarthi et al., 2002). The black line denotes the profile location in Figure 10. The depth is in kilometers.



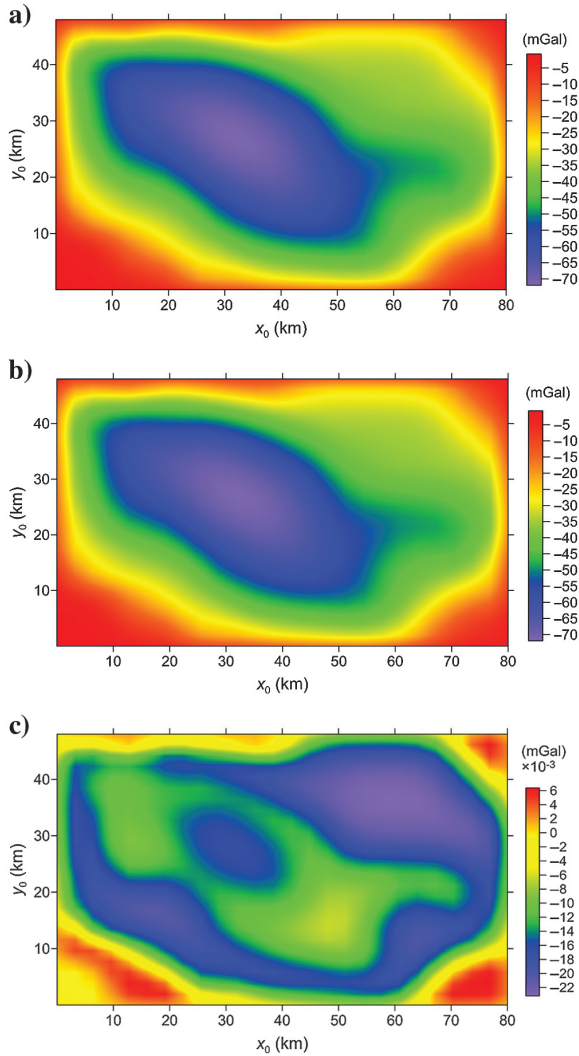


Figure 9. Gravity anomaly contour maps in Los Angeles Basin, calculated using (a) our analytic solution, (b) solution 1, and (c) their differences. The anomalies and their differences are in milligals.

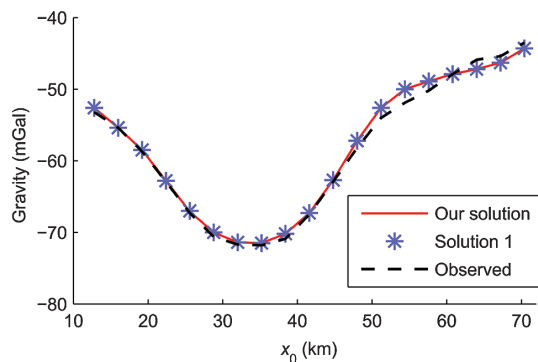


Figure 10. Gravity anomaly curves along the profile in Figure 8. The solid line denotes the anomalies calculated using our solution, stars denote the anomalies calculated using solution 1, and the dashed line denotes the observed residual gravity anomalies from Chakravarthi et al. (2002).

the prism. Point E is on an edge of the top facet of the prism. Points G, H, and I are, respectively, inside, on the bottom facet of, and below the prism, imitating the borehole observation. Among them, D, E, F, G, and H are located at points causing singularities for the analytic solutions.

The analytic solution of gravity anomaly of a uniform prism is well-known, and its singularity has been solved (Li and Chouteau, 1998; Nagy et al., 2000). From the error curve in Figure 7, the gravity anomaly using solution 2 with 50 uniform subprisms divided from the prism in Figure 5 nearly equals the true gravity anomaly of the prism. So the gravity anomalies at the nine points were computed using solution 2 with 50 uniform subprisms, denoted with  $\Delta g_2$  in Table 3. Also, the gravity anomalies at the nine points, denoted with  $\Delta g_1$  in Table 3, were computed using our analytic solution for the prism with the fourth-order polynomial density contrast. The differences,  $\Delta g_1 - \Delta g_2$ , between the two gravity anomalies at the nine points were also listed in Table 3. We can see that wherever the computation points locate, the differences are very little; i.e., the gravity anomalies obtained using our solution coincide quite well with those using solution 2. Consequently, our analytic solution can be used to compute gravity anomalies of bodies without singularities at points within the range of numerical stability.

### 3D basin case

A right-rectangular prism, as a versatile geometric representation, has played a significant role in gravity modeling of 3D bodies, especially over a wide range of sedimentary basins. Here, we apply our analytic solution to model gravity anomalies in the Los Angeles Basin in California. Chai and Hinze (1988) obtain the gravity anomalies of the basin assuming exponential density-depth function. Later, Chakravarthi et al. (2002) complete it using their analytic solution of a prism with parabolic density-contrast variation in Table 1. We have the fourth-order polynomial density-contrast function in Table 1 by fitting the parabolic density-contrast function.

We obtained the basement depth of the Los Angeles Basin, shown in Figure 8, by digitizing the depth-contour map of the basement interface from Chakravarthi et al. (2002) with  $0.8 \times 0.8$  km<sup>2</sup> grid. The basin was approximated using 625 prisms, and each prism is 3.2 km in the  $x$ -direction and 1.92 km in the  $y$ -direction. We then computed the gravity anomalies of the basin using our analytic solution and solution 1, respectively. Figure 9a shows the gravity anomalies using our solution, Figure 9b shows those using solution 1, and Figure 9c shows their differences. The rms error between the two anomalies is  $1.38 \times 10^{-2}$  mGal, a negligible amount relative to the gravity anomaly values.

Figure 10 shows the gravity anomaly curves along the profile line, shown by the black line in Figure 8. The dashed curve denotes the observed residual gravity anomaly (Chakravarthi et al., 2002), and the solid curve and stars denote the gravity anomalies computed by our solution and solution 1, respectively. It can be seen from Figures 9 and 10 that the two anomalies computed are almost coincident with each other and fairly close to the observed anomaly. These consistencies further validate our analytic solution.

### CONCLUSION

We have proposed a versatile analytic solution of gravity anomalies of a right-rectangular prism with a general polynomial density-contrast function of depth. The solution is singularity free in the

upper half-space over the prism. Singularities existing in the lower half-space containing the prism are resolved by assigning limits to the singular terms in the corresponding expressions, and thus the gravity anomalies can be computed without numerical singularities at any point (outside, inside, or on the facets of the prism). Numerical stability tests indicate the stability range of our solution decreases with increase of the order of polynomial density-contrast function. For practical applications, the lowest order polynomial giving an adequate density contrast representation should be used, to keep the stability range of our solution as large as possible.

An arbitrary-order polynomial function, due to its generalization and flexibility, can well-approximate the complicated density-contrast variation of an inhomogeneous geologic body, which is especially appropriate for sediments filling basins. Our solution can be regarded as a generalization of analytic solutions for gravity anomalies of a prism with other density-contrast functions of depth, such as linear, hyperbolic, parabolic, and exponential functions.

Because 3D irregular bodies can be approximated by a collection of finite-juxtaposed prisms, our solution is applicable to 3D irregular bodies with complicated density-contrast variation at points within the numerical stability range. Our solution can also greatly improve the computational efficiency and accuracy of gravity anomaly computations for variable density-contrast bodies against the common solution of summing the effects of a collection of uniform prisms. Moreover, our solution of the variable density-contrast prism is also superior to that of a uniform prism for gravity inversion, such as the determination of a basement interface from gravity data.

## ACKNOWLEDGMENTS

We sincerely thank the editor M. Sacchi, assistant editor J. Etgen, reviewers M. Zhdanov, J. Bain, and H. Holstein, and the associate editor for their constructive comments and suggestions, which helped to significantly improve this paper. This work was supported by the National Natural Science Foundation of China (grant nos. 41074077 and 41230318) and the Specialized Research Fund for the Doctoral Program of Higher Education (grant no. 20130132110023).

## REFERENCES

- Athy, L. F., 1930, Density, porosity, and compaction of sedimentary rocks: AAPG Bulletin, **14**, 1–24.
- Chai, Y. F., and W. J. Hinze, 1988, Gravity inversion of an interface above which the density contrast varies exponentially with depth: *Geophysics*, **53**, 837–845, doi: [10.1190/1.1442518](https://doi.org/10.1190/1.1442518).
- Chakravarthi, V., H. M. Raghuram, and S. B. Singh, 2002, 3-D forward gravity modeling of basement interfaces above which the density contrast varies continuously with depth: *Computers & Geosciences*, **28**, 53–57, doi: [10.1016/S0098-3004\(01\)00080-2](https://doi.org/10.1016/S0098-3004(01)00080-2).
- Chakravarthi, V., S. R. Sastry, and B. Ramamma, 2013, MODTOHAFSD: A GUI based JAVA code for gravity analysis of strike limited sedimentary basins by means of growing bodies with exponential density contrast-depth variation: A space domain approach: *Computers & Geosciences*, **56**, 131–141, doi: [10.1016/j.cageo.2013.02.005](https://doi.org/10.1016/j.cageo.2013.02.005).
- Chappell, A., and N. Kusznir, 2008, An algorithm to calculate the gravity anomaly of sedimentary basins with exponential density-depth relationships: *Geophysical Prospecting*, **56**, 249–258, doi: [10.1111/gpr.2008.56.issue-2](https://doi.org/10.1111/gpr.2008.56.issue-2).
- Commer, M., 2011, Three-dimensional gravity modeling and focusing inversion using rectangular meshes: *Geophysical Prospecting*, **59**, 966–979, doi: [10.1111/j.1365-2478.2011.00969.x](https://doi.org/10.1111/j.1365-2478.2011.00969.x).
- D'Urso, M. G., 2013, On the evaluation of the gravity effects of polyhedral bodies and a consistent treatment of related singularities: *Journal of Geodesy*, **87**, 239–252, doi: [10.1007/s00190-012-0592-1](https://doi.org/10.1007/s00190-012-0592-1).
- D'Urso, M. G., 2014, Gravity effects of polyhedral bodies with linearly varying density: *Celestial Mechanics and Dynamical Astronomy*, **120**, 349–372, doi: [10.1007/s10569-014-9578-z](https://doi.org/10.1007/s10569-014-9578-z).
- D'Urso, M. G., 2015, The gravity anomaly of a 2D polygonal body having density contrast given by polynomial functions: *Surveys in Geophysics*, **36**, 391–425, doi: [10.1007/s10712-015-9317-3](https://doi.org/10.1007/s10712-015-9317-3).
- Gallardo-Delgado, L. A., M. A. Pérez-Flores, and E. Gómez-Treviño, 2003, A versatile algorithm for joint 3D inversion of gravity and magnetic data: *Geophysics*, **68**, 949–959, doi: [10.1190/1.1581067](https://doi.org/10.1190/1.1581067).
- García-Abdeslem, J., 1992, Gravitational attraction of a rectangular prism with depth-dependent density: *Geophysics*, **57**, 470–473, doi: [10.1190/1.1443261](https://doi.org/10.1190/1.1443261).
- García-Abdeslem, J., 2005, The gravitational attraction of a right rectangular prism with density varying with depth following a cubic polynomial: *Geophysics*, **70**, no. 6, J39–J42, doi: [10.1190/1.2122413](https://doi.org/10.1190/1.2122413).
- Gokula, A. P., and R. G. Sastry, 2015, Gravitational attraction of a vertical pyramid model of flat top-and-bottom with depth-wise parabolic density variation: *Journal of Earth System Science*, **124**, 1735–1744, doi: [10.1007/s12040-015-0633-2](https://doi.org/10.1007/s12040-015-0633-2).
- Guo, Z. H., Z. N. Guan, and S. Q. Xiong, 2004, Cuboid  $\Delta T$  and its gradient forward theoretical expressions without analytic odd points: *Chinese Journal of Geophysics*, **47**, 1277–1285, doi: [10.1002/cjg2.v47.6](https://doi.org/10.1002/cjg2.v47.6).
- Hansen, R. O., 1999, An analytical expression for the gravity field of a polyhedral body with linearly varying density: *Geophysics*, **64**, 75–77, doi: [10.1190/1.1444532](https://doi.org/10.1190/1.1444532).
- Holstein, H., 2003, Gravimagnetic anomaly formulas for polyhedra of spatially linear media: *Geophysics*, **68**, 157–167, doi: [10.1190/1.1543203](https://doi.org/10.1190/1.1543203).
- Holstein, H., D. Hillan, D. Fitzgerald, and C. Foss, 2014, Numerical stability control in magnetic gradient calculations of a discretized cylinder: 6th Saint Petersburg International Conference and Exhibition, EAGE, Extended Abstracts, doi: [10.3997/2214-4609.20140300](https://doi.org/10.3997/2214-4609.20140300).
- Holstein, H., and B. Ketteridge, 1996, Gravimetric analysis of uniform polyhedra: *Geophysics*, **61**, 357–364, doi: [10.1190/1.1443964](https://doi.org/10.1190/1.1443964).
- Kwok, Y. K., 1991, Singularities in gravity computation for vertical cylinders and prisms: *Geophysical Journal International*, **104**, 1–10, doi: [10.1111/gji.1991.104.issue-1](https://doi.org/10.1111/gji.1991.104.issue-1).
- Li, X., and M. Chouteau, 1998, Three-dimensional gravity modeling in all space: *Surveys in Geophysics*, **19**, 339–368, doi: [10.1023/A:1006554408567](https://doi.org/10.1023/A:1006554408567).
- Litinsky, V. A., 1989, Concept of effective density: Key to gravity depth determinations for sedimentary basins: *Geophysics*, **54**, 1474–1482, doi: [10.1190/1.1442611](https://doi.org/10.1190/1.1442611).
- Nagy, D., 1966, The gravitational attraction of a right rectangular prism: *Geophysics*, **31**, 362–371, doi: [10.1190/1.1439779](https://doi.org/10.1190/1.1439779).
- Nagy, D., G. Papp, and J. Benedek, 2000, The gravitational potential and its derivatives for the prism: *Journal of Geodesy*, **74**, 552–560, doi: [10.1007/s001900000116](https://doi.org/10.1007/s001900000116).
- Prutkin, I., and R. Tenzer, 2009, The optimum expression for the gravitational potential of polyhedral bodies having a linearly varying density distribution: *Journal of Geodesy*, **83**, 1163–1170, doi: [10.1007/s00190-009-0334-1](https://doi.org/10.1007/s00190-009-0334-1).
- Rao, C. V., M. L. Raju, and V. Chakravarthi, 1995, Gravity modeling of an interface above which the density contrast decreases hyperbolically with depth: *Journal of Applied Geophysics*, **34**, 63–67, doi: [10.1016/0926-9851\(94\)00057-U](https://doi.org/10.1016/0926-9851(94)00057-U).
- Rao, D. B., 1990, Analysis of gravity anomalies of sedimentary basins by an asymmetrical trapezoidal model with quadratic density function: *Geophysics*, **55**, 226–231, doi: [10.1190/1.1442830](https://doi.org/10.1190/1.1442830).
- Rao, D. B., M. J. Prakash, and N. R. Babu, 1990, 3D and 2½ D modeling of gravity anomalies with variable density contrast: *Geophysical Prospecting*, **38**, 411–422, doi: [10.1111/gpr.1990.38.issue-4](https://doi.org/10.1111/gpr.1990.38.issue-4).
- Roussel, C., J. Verdun, J. Cali, and F. Masson, 2015, Complete gravity field of an ellipsoidal prism by Gauss-Legendre quadrature: *Geophysical Journal International*, **203**, 2220–2236, doi: [10.1093/gji/ggv438](https://doi.org/10.1093/gji/ggv438).
- Tsouli, D., and S. Petrovic, 2001, On the singularities of the gravity field of a homogeneous polyhedral body: *Geophysics*, **66**, 535–539, doi: [10.1190/1.1444944](https://doi.org/10.1190/1.1444944).
- Verweij, J. M., T. A. P. Boxem, and S. Nelskamp, 2016, 3D spatial variation in vertical stress in on- and offshore Netherlands: Integration of density log measurements and basin modeling results: *Marine and Petroleum Geology*, **78**, 870–882, doi: [10.1016/j.marpetgeo.2016.06.016](https://doi.org/10.1016/j.marpetgeo.2016.06.016).
- Wu, L. Y., and L. W. Chen, 2016, Fourier forward modeling of vector and tensor gravity fields due to prismatic bodies with variable density contrast: *Geophysics*, **81**, no. 1, G13–G26, doi: [10.1190/geo2014-0559.1](https://doi.org/10.1190/geo2014-0559.1).
- Zhang, J. Z., B. S. Zhong, X. X. Zhou, and Y. Dai, 2001, Gravity anomalies of 2-D bodies with variable density contrast: *Geophysics*, **66**, 809–813, doi: [10.1190/1.1444970](https://doi.org/10.1190/1.1444970).
- Zhou, X. B., 2009, 3D vector gravity potential and line integrals for the gravity anomaly of a rectangular prism with 3D variable density contrast: *Geophysics*, **74**, no. 6, I43–I53, doi: [10.1190/1.3239518](https://doi.org/10.1190/1.3239518).
- Zhou, X. B., 2010, Analytic solution of the gravity anomaly of irregular 2D masses with density contrast varying as a 2D polynomial function: *Geophysics*, **75**, no. 2, I11–I19, doi: [10.1190/1.3294699](https://doi.org/10.1190/1.3294699).
- Zwillinger, D., 2011, CRC standard mathematical tables and formulae, 32nd ed.: CRC Press.